Study of nanocomposites based on cellulose nanoparticles and natural rubber latex by ATR/FTIR spectroscopy: The impact of reinforcement: The impact of reinforcement

5 authors, including:

Agrebi Fatma
Université de Picardie Jules Verne
3 PUBLICATIONS   **3** CITATIONS

SEE PROFILE

Serge Bresson
Université de Picardie Jules Verne
24 PUBLICATIONS   **216** CITATIONS

SEE PROFILE

Nouha Ghorbel
University of Sfax
17 PUBLICATIONS   **56** CITATIONS

SEE PROFILE

Ouissam Abbas
Walloon Agricultural Research Centre CRA-W
58 PUBLICATIONS   **611** CITATIONS

SEE PROFILE

Some of the authors of this publication are also working on these related projects:

Project   Hybrid Materials for Optical and Optoelectronic Applications View project

Project   Synthesis of new ILs and their spectroscopy analysis, View project

Study of Nanocomposites Based on Cellulose Nanoparticles and Natural Rubber Latex by ATR/FTIR Spectroscopy: The Impact of Reinforcement

Fatma Agrebi [ORCID],[1,2] **Nouha Ghorbel,**[1] **Serge Bresson,**[2] **Ouissam Abbas,**[3] **Ali Kallel**[1]
[1]*LaMaCoP, Faculty of Sciences of Sfax, University of Sfax, BP, 3018, Sfax, Tunisia*

[2]*Laboratoire de Physique des Systèmes Complexes, Université Picardie Jules Verne, Amiens, France*

[3]*Walloon Agricultural Research Centre (CRA-W), Valorisation of Agricultural Products, Department, Food and Feed Quality Unit (U15), 'Henseval Building', Chaussée de Namur 24, 5030, Gembloux, Belgium*

In materials research, polymer nanocomposites have attracted great attention worldwide from both academic and industrial points of view. The material properties of polymers can be enhanced dramatically by incorporating nanoelements from renewable resources depending on their biological origin (e.g., cellulose, starch, and chitin). We have used as the reinforcing phase in this work, cellulose nanowhiskers (CNWs) and nanofibrillated cellulose (NFC) to prepare nanocomposite films by casting/evaporation using natural rubber (NR) latex as the matrix. Our interest is focused, in this work, especially on the investigation of the chemical bonds of the NR matrix and the chemical links of nanowhiskers added to the matrix and therefore the physical and chemical interactions which could happen between the reinforcement and the matrix. Many techniques have been used to explore the interface. Among these techniques, attenuated total reflectance/Fourier transform infrared spectroscopy (ATR/FTIR), which is employed in this work. It is exhibited that some differences are observed in FTIR spectra of nanocomposite films when adding cellulose nanoparticles into NR matrix. Overall IR spectroscopy clearly demonstrated that the interfacial adhesion in the case of NR-NFC nanocomposite is higher than that of NR-CNW one which was explained by the presence of residual lignin at the NFC surface that play the role of "compatibilizing" agent that enhance the adhesion between the NFC and the NR. POLYM. COMPOS., 2018. © 2018 Society of Plastics Engineers

INTRODUCTION

In recent years, enormous efforts have been made to develop, characterize, and utilize bio-based materials, and bio-based nanocomposites belong to the new generation of biobased materials [1,2]. Cellulose is the most abundant biomass on the earth and its use in the preparation of bio-based nanomaterials has gained a growing interest during the last 10 years. It is one of the best natural materials to generate nanofillers for producing nanocomposites with good performance, including the chemical compatibility between nanofiller and the polymeric matrix that plays a major role in both the dispersion of particles in the matrix and the adhesion between these phases [3]. In this study, nanofibrillated cellulose (NFC) and cellulose nanowhiskers (CNWs) were used as reinforcing phase to prepare nanocomposite films by casting/evaporation using latex of natural rubber (NR) as matrix. The choice of the matrix was dictated by the fact that it is a natural polymer, often reinforced with nanoparticles and available as latex [4].

In the nanocomposites, CNWs and NFCs are nanoscale cellulose fibers that can exert significant effect on the matrix polymer due to their different composition, shape and size.

One of the goals of this article is to compare their morphologies, crystalline structure and outline the major factors that might be influencing the interactions with latex (NR) matrix and the resulting reinforcing effects on the matrix polymer. Numerous studies have been carried out using various cellulosic nanofibers for polymer reinforcement [5–7]. These studies dealt with the thermal, mechanical and dielectric behavior of NR-NFC and NR-CNW nanocomposites. By studying two different types of fibers, it was found that the interfacial adhesion is higher for NR/NFC nanocomposite compared with NR/CNW. In fact, residual lignin and hemicelluloses surrounding NFC increase the tensile modulus and decrease the deformation at break. These impurities thus improve the interfacial adhesion between fibers and matrix. Moreover, it has been noted that the storage modulus is higher and the damping factor tanδ is lower for NR-NFC compared with NR-CNW.

In spite of all previous studies, a greater clarity is still needed on the reinforcing effects of different cellulose nanofibers. attenuated total reflectance/Fourier transform infrared spectroscopy (ATR/FTIR) spectroscopy is a complementary technique that can provide a sensitive, relatively quick, non-destructive means of probing molecular structure in our nanocomposite films [8–11]. Such technique is used here to examine the above-mentioned properties of nanocellulose fibers and nanocomposites.

Furthermore, ATR/FTIR is convenient for analysis of conformational dependence, and intra- and inter-chain interactions [12]. In fact, it is well known that the different surface properties between the nanofiber and the NR matrix, that is, the former is highly polar and hydrophilic while the latter is, generally, non-polar and relatively hydrophobic, impose the modification of the fibers surface or the addition of compatibilizing agents, in order to improve the fiber/polymer compatibility and their interfacial adhesion. In this context, lignin which contains both polar and nonpolar groups [13] and located at the NFC surface, acts as a coupling agent linking hydrophilic cellulose with the hydrophobic NR matrix, and thus, it can enhance interfacial compatibility between the fibers and polymer matrix. So, we draw attention in this article to the reinforcing efficiency of nanocellulose in the nanofibers/matrix interfacial adhesion. The results from this study show clearly that for the same nanocellulose concentration, distinctions between short rigid CNWs and long relatively tough NFCs in terms of their reinforcing effects, thus providing a practical supervision for the progress of polymer nanocomposites containing cellulose nanofibers. A comparative study will be interesting and informative for determining the nanocomposite which has the best adhesion properties.

EXPERIMENTAL

Materials

NR extracted from tropical trees of the species of Hevea Brasiliens. It was provided by Michelin (Clermont Ferrand France). It contained spherical particles with diameter about 1 μm and its concentration was about 31 wt%. The density of dry NR, ρ_{NR}, was 1 g. cm^{-1} with >97% of cis-1,4-polyisoprene.

Cellulose is among the most abundant materials in nature; its structure is composed of b-D-glucopyranose repeating units linked by (1–4)-glycosidic bonds. The NFC and CNW were extracted from the rachis of date palm tree as described elsewhere [14]. CNWs and NFCs show substantially different sizes as seen in the Transmission electron microscopy micrographs for CNWs and NFCs [5,15]. CNWs are rigid cellulose rods with an average width less than 10 nm and an average length of 100–400 nm while NFCs are flexible filaments with an average width of 8–12.5 nm and an average length of 700–1,100 nm. NFCs are obtained by mechanical treatment (the bleached

cellulose was disintegrated by pumping through a micro-fluidizer processor [Model M-110EH-30]) whereas it is a chemical process that leads to the formation of CNWs (chemical treatment [hydrolysis] is applied to remove the amorphous regions of the cellulose polymer). Then, the resulting nanoparticles (CNW/NFC) were used as reinforcing phase to prepare nanocomposite films using latex of NR as matrix, following the protocol given by Bendahou et al. [15]. The mixture was stirred using a magnetic stirrer for 8 h and then placed in a rotary evaporator for degassing, to avoid the presence of air bubbles in the dry films. It is then poured into a Petri dish covered with Polytetra-fluoroethyle (PTFE) and placed in a ventilated oven at 40°C for 2–3 days depending on the filler content in the film. Further drying of the films was performed for 12 h under vacuum at 40°C.

On the basis of this investigation, the matrix NR and various nanocomposites based on both NFC NR-NFC1, NR-NFC2.5, NR-NFC7.5, NR-NFC10, and NR-NFC15 and CNWs NR-CNW1, NR-CNW2.5, NR-CNW5, NR-CNW7.5, and NR-CNW15 were investigated, where the digits indicate the nanoparticle content, in weight.

ATR/FTIR Measurements

The measurements were realized in the Walloon Agricultural Research Center (Cra-w) Belgium. All ATR/FTIR spectra were recorded on a Vertex 70-RAM II Bruker spectrometer (Bruker Analytical,Madison, WI) operating with a Golden Gate TM diamond ATR accessory (Specac Ltd, Slough, UK). FTIR/ATR spectra [4,000–500 cm^{-1}] were collected with resolution of 4 cm^{-1} by co-adding 256 scans for each spectrum at room temperature. The OPUS 6.0 software for windows of Bruker Instruments was used for instrument management.

RESULTS AND DISCUSSION

Vibrational Analysis of the NR Matrix

FTIR/ATR spectrum (4,000–600 cm^{-1}) of NR matrix is illustrated in Fig. 1a. The assignments of the observed modes in this spectral region are reported in Table 1. All reported peak values were based on the maximum peak height of the unfitted spectra. Curve fitting and fitted frequency values labeled * were performed as per Bresson et al. [16]. We can note that the position of the peaks of NR matrix spectrum is similar to those described stufly by different authors [17–19]. On the IR spectrum (see Fig. 1a), we distinguish four well defined spectral regions: 3,500–2,600, 1,800–1,500, 1,500–1,200, and 1,200–600 cm^{-1}.

Region 3,500–2,600 cm^{-1}. In this spectral region, we observe the affected modes of alkyl stretchable region alcohol OH (3,500–3,100 cm^{-1}) and ν(C-H) stretching region (3,100–2,600 cm^{-1}). In The CH stretching region, we
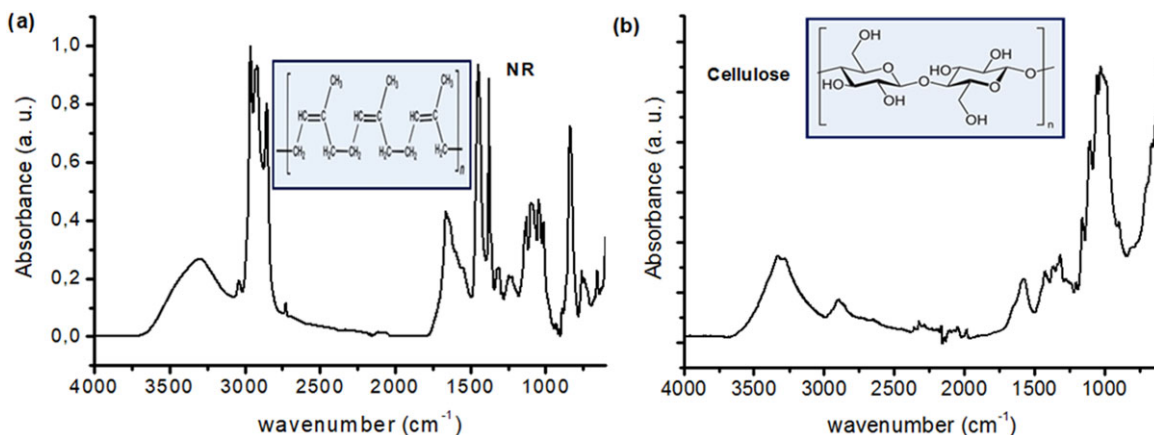
FIG. 1. IR spectra of (a) NR matrix and (b) cellulose in the spectral range 600–4,000 cm^{-1} [Color figure can be viewed at wileyonlinelibrary.com]

observe several peaks at: 3,042, 2,988, 2,962, 2,932, 2,913, 2,881, 2,852, 2,725 cm^{-1} [20]. Four peaks dominate in intensity the spectrum: 2,962, 2,932, 2,913, and 2,852 cm^{-1} assigned to CH$_3$ symmetric stretching modes for the first three and CH$_2$ antisymmetric stretching modes for the last.

For the spectral region 3,500–3,100 cm^{-1}, we observe a wide peak which can be used to adjust by three Lorentzian functions centered at 3,450, 3,350, and 3,140 cm^{-1}. The appearance of these modes in this IR spectrum is the signature of the presence of water in our NR sample.

TABLE 1. Observed FTIR/ATR bands and their assignment of NR and cellulose.

NR	Cellulose	ASSIGNMENT	NR	Cellulose	ASSIGNMENT
Zone 1,200–800			**Zone 1,500–1,200**		
				1,202 (m)	ν(C-O-C)
	814* (w)	ρ(CH$_2$)	1,220* (w)	1,232 (m)	τ(CH$_2$)
841 (s)		ρ(CH$_3$)			
864* (sh)		ρ(CH$_2$)	1,246* (w)	1,255* (w)	τ(CH$_2$)
889* (w)	895* (w)	ρ(CH$_2$)			
930* (w)		ρ(CH$_3$)	1,307 (m)	1,314 (s)	δ(CH)/ δ(OH)
982* (sh)		ρ(CH$_3$)			δ(CH)
1,013 (m)	014 (m)	ν(C-C)	1,322 (m)	1,337 (m)	δ(OH)
1,036* (sh)	1,030 (m)	ν(C-C)/ν(C-O)			δ(CH$_3$)
1,048 (m)		ν(C-C)	1,360 (m)	1,372 (m)	δ(CH$_3$) + δ(CH)
	1,055 (m)	ν(C-O)	1,376 (s)		
1,065* (sh)		ν(C-C)	1,401* (sh)	1,405* (sh)	δ(CH$_2$)
1,080 (m)		ν(C-C)			
1,100* (sh)	1,107 (m)	ν(C-C)	1,434* (sh)	1,426 (m)	δ(CH$_2$)
1,126 (m)		ν(C-C)			
1,140* (sh)		ν(C-C)	1,450 (s)	1,454* (sh)	δ(CH$_2$)
Zone 1,800–1,500			**Zone 4,000–2,700**		
1,511* (sh)		δ(H$_2$O)	2,725* (w)		ν(C-H)
1,543 (m)			2,852 (s)	2,851 (m)	ν_s(CH$_2$)
		δ(H$_2$O)	2,881* (sh)		ν_{as}(CH$_2$)
	1,564* (sh)		2,913 (m)	2,901* (sh)	ν_{as}(CH$_2$)
		δ(O-H)	2,932 (m)		ν_s(CH$_3$)
1,586* (sh)			2,962 (s)		ν_s(CH$_3$)
		δ(H$_2$O)	2,988* (sh)		ν_s(CH$_3$)
	1,595 (m)		3,042* (w)		ν_{as}(CH$_3$)
		δ(O-H)	3,140* (w)		ν(=C-H)
				3,160* (sh)	ν(O-H)
1,634 (s)		ν(C=C)		3,271 (s)	ν(O-H)
				3,325 (s)	ν(O-H)
	1,653* (sh)	δ(O-H)			ν(O-H)
			3,350* (w)		ν(O-H)
1,664 (s)		ν(C=C)	3,450* (sh)	3,424* (sh)	ν(O-H)

w, weak; m, medium; s, strong; sh, shoulder; ν, Str, stretch; δ, bending deformation; τ, twisting; ρ, rocking; s, symmetric; as, antisymmetric; *, fitted values.
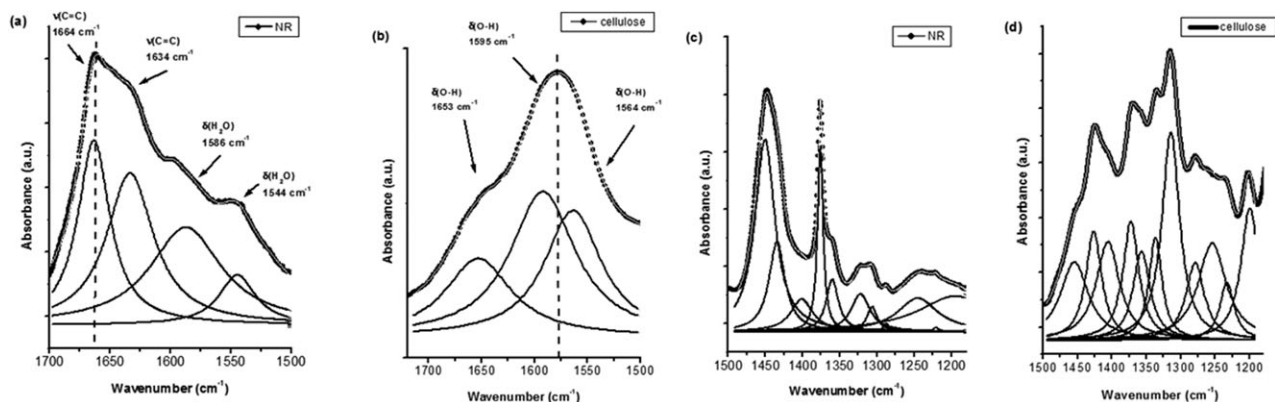
FIG. 2. IR spectra of (a) NR matrix and (b) cellulose in the spectral range 1,500–1,800 cm^{-1} and (c) NR matrix and (d) Cellulose in the spectral range 1,200–1,500 cm^{-1} fitted by Lorentzian curves.

Region 1,800–1,500 cm^{-1}. In this spectral zone (Fig. 2a), we observe a wide peak with a maximum at 1,664 cm^{-1} and three shoulders at 1,634, 1,586, and 1,544 cm^{-1}. The peaks at 1,664 and 1,634 cm^{-1} are assigned to ν(C=C) stretching modes whereas the modes at 1,586 and 1,544 cm^{-1} correspond to δ (H_2O) deformation revealing the presence of water which is connected to the hydroxyl groups (-OH) of the lipid present in our sample [5].

Region 1,500–1,200 cm^{-1}. In this spectral zone (Fig. 2c), we observe numerous more and less defined peaks. The number of adjusted components by Lorentzian functions is important. This spectral region is dominated by the CH, CH$_2$, and CH$_3$ deformations (1,500–1,300 cm^{-1}) and the CH$_2$ twisting modes (1,300–1,200 cm^{-1}) [20]. Two peaks have an important intensity: 1,450 cm^{-1} assigned to δ (CH$_2$) deformation and 1,376 cm^{-1} assigned to δ (CH$_3$) deformation.

Region 1,200–600 cm^{-1}. In this spectral zone (Fig. 1a), we observe four intense peaks at 1,126, 1,080, 1,048, and 841 cm^{-1}. The first three peaks are assigned to the C-C stretching modes whereas the last peak corresponds to the CH$_3$ rocking mode [20].

Vibrational Analysis of The Reinforcement (Cellulose)

The attribution of various bands of the cellulose bands spectrum has been the subject of numerous studies. The works of Marechal and Chanzy describe in detail the different bands forming a spectrum of cellulose [21].

Figure 1b shows our FTIR spectrum of cellulose. The main absorbance peaks obtained for cellulose are as follows: the broad band at 3,200–3,355 cm^{-1} which corresponds to the stretching vibration of OH groups of cellulose. In general, this group can come from lignin, hemicelluloses, cellulose and pectin. In this spectral region, we observe a wide band with two visible peaks at 3,325 and 3,271 cm^{-1}. In the spectra region 3,100–2,700 cm^{-1}, the bands at 2,901 and 2,851 cm^{-1} characterize the methylene C-H asymmetric and

symmetric stretching vibration, respectively [22]. In the spectral region 1,800–1,500 cm^{-1} we observe in Fig. 2b a wide band centered at 1,595 cm^{-1} attributed to the bending mode of the absorbed water [23]. In the spectral region 1,500–1,200 cm^{-1}, we observe in Fig. 2d numerous more or less intense peaks. The absorbance at 1,337 and 1,314 cm^{-1} are assigned to the bending of hydroxyl group –OH in cellulose [24,25]. In the spectral region 1,200–600 cm^{-1}, the bands at 1,202, 1,055, and 1,030 cm^{-1} are assigned to the elongation of C-O bonds in alcohol and other functions [20,24,26].

In comparison with the NR IR spectrum, we can note the existence of vibrational modes characteristics of each of both elements constituting the NR reinforced by the cellulose:

- For NR, we have the ν(C=C) stretching modes at 1,664 and 1,634 cm^{-1} and ρ(CH$_3$) rocking modes at 841 cm^{-1},
- For cellulose, we have more vibrational signatures: the ν(O-H) stretching modes at 3,325 and 3,271 cm^{-1}, the δ(O-H) bending modes at 1,595, 1,337, and 1,314 cm^{-1} and ν(C-O) stretching modes at 1,202, 1,055, and 1,030 cm^{-1}.

Vibrational Analysis of Nanocomposites

Now due to incorporation of different amounts of cellulose nanofibres into NR matrix, some differences can be observed in FTIR spectra of nanocomposites films.

In the Spectral Region 3,500–2,600 cm^{-1}. In Fig. 3a and c, where both spectra were normalized on the mode at 3,035 cm^{-1}, we present the FTIR spectra of NR-CNW and NR-NFC nanocomposites according to the rate of cellulose reinforcement inside the NR matrix. The adjustment was made by curve fitting with software Origin 7 using a combination of lorentzian functions, according to reinforcement rate between 1 and 15% of cellulose.

The assignments of the observed modes in spectral region 4,000–800 are reported in Table 2 for NR-CNW samples and in Table 3 for NR-NFC samples. All reported peak values were based on the maximum peak height of
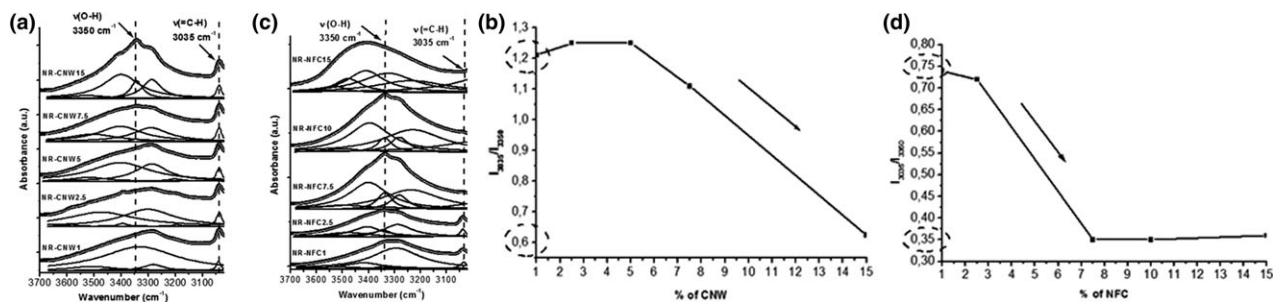
FIG. 3. IR spectra of (a) NR-CNW and (c) NR-NFC nanocomposites fitted by Lorentzian curves as a function of reinforcement rate in the spectral region from 2,600 to 3,500 cm^{-1} and the intensity ratio $I_{3,035}/I_{3,350}$ as a function of reinforcement rate for (b) NR-CNW and (d) NR-NFC nanocomposites.

the unfitted spectra. Curve fitting and fitted frequency values labeled * were performed as per Bresson et al. [16]. When compared with pure NR which exhibits a broad stretching peak centered at 3,350 cm^{-1}, the peaks of NR-CNW and NR-NFC corresponding to the ν(O-H) stretching modes are much sharper and stronger, indicating higher densities of the hydroxyl groups on the surfaces of CNW and NFC [27].

In general on the Fig. 3a and c, we have four adjusted components by Lorentzian functions between 3,100 and 3,600 cm^{-1}, ascribed to intramolecular and intermolecular hydrogen bonding [28,29]. According to the rate of cellulose reinforcement, we observe that the intensity of the ν(O-H) stretching modes for NR-NFC samples evolves in a more important way than for the case of the NR-CNW samples. We can note a similarity between the NR-CNW 15% spectrum and that of NR-NFC 7.5%. Table 4 is a summary of changes in functional group band intensity for

NR-CNW and NR-NFC. Moreover, for the NR-NFC 15%, we remark a shift of peaks towards higher IR frequencies which comes along with a very important increase in intensity. These phenomena indicate important effects of the cellulose nanofibers on the NR matrix through hydrogen bonding, and lesser effects in the case of NR-CNW in comparison with NR-NFC structure.

In addition, we observe a strong variation of intensity between the peaks at 3,035 and 3,350 cm^{-1}, corresponding respectively to asymmetric = C-H stretching vibration related to NR matrix and O-H stretching vibration which characterize the hydrogen bonds that can take place between NR matrix and cellulose nanofibers or nanowhiskers. Figure 4b and d shows the intensity ratio $I_{3,035}/I_{3,350} = I_{\nu(=\text{C-H})}/I_{\nu \text{ (C-OH)}}$ according to the percentage of cellulose for NR-CNW and NR-NFC respectively. We note that for NR reinforced with CNWs, we have a little influence of reinforcement rates, so there are no hydrogen bonds between 1 and 7.5% of CNW

TABLE 2. Observed FTIR / ATR bands and their assignment of NR reinforced by CNWs (NR-CNW).

NR-CNW 1%	NR-CNW 2.5%	NR-CNW 5%	NR-CNW 7.5%	NR-CNW 15%	Assignement
Zone	**1,500–1,200**				
1,206* (sh)	1,207* (sh)	1,207* (sh)	1,203* (sh)	1,202* (sh)	ν(C-O-C)
1,245 (w)	1,257 (m)	1,245 (m)	1,244 (m)	1,241 (m)	τ(CH$_2$)
		1,285 (w)	1,284 (w)	1,283 (w)	τ(CH$_2$)
1,313 (w)	1,307 (m)	1,308 (m)	1,309 (m)	1,314 (m)	δ(CH)/ δ(OH)
	1,323* (sh)	1,325* (sh)	1,328* (sh)	1,336* (sh)	δ(CH)
1,360 (m)	1,359 (m)	1,359 (m)	1,358 (m)	1,358 (m)	δ(CH$_3$)
1,375 (s)	1,375 (s)	1,375 (s)	1,375 (s)	1,375 (s)	δ(CH$_3$)
1,403* (sh)	1,403* (sh)	1,403* (sh)	1,403* (sh)	1,403* (sh)	δ(CH$_3$) + δ(CH)
1,432* (m)	1,434* (m)	1,433* (m)	1,435* (m)	1,433* (sh)	δ(CH$_2$)
1,447* (s)	1,451* (s)	1,448* (s)	1,451* (s)	1,448 (s)	δ(CH$_2$)
Zone	**1,800–1,500**				
1,541 (m)	1,538 (m)	1,521* (w)	1,521* (sh)	1,541 (m)	δ(0-H)
1,576 (m)	1,568 (m)	1,547 (m)	1,544 (m)	1,577 (m)	δ(0-H)
		1,620 (m)	1,585 (m)	1,596 (m)	δ(0-H)
1,644* (sh)	1,645 (m)	1,638 (m)	1,642 (m)	1,634 (m)	ν(C=C)
1,663 (m)	1,664 (m)	1,662 (m)	1,664 (m)	1,663 (m)	ν(C=C)
Zone	**4,000–3,000**				
3,035 (m)	3,037 (m)	3,038 (m)	3,038 (m)	3,038 (m)	ν(=C-H)
3,200* (sh)	3,100* (sh)	3,201* (sh)	3,290 (m)	3,287 (m)	ν(O-H)
3,284 (m)	3,300 (m)	3,290 (m)	3,346* (w)	3,343 (m)	ν(O-H)
3,350* (w)	3,395* (w)	3,400 (m)	3,400 (m)	3,400 (m)	ν(O-H)
3,503* (sh)	3,505* (sh)	3,515* (sh)	3,510* (sh)	3,520* (sh)	ν(O-H)

TABLE 3. Observed FTIR/ATR bands and their assignment of NR reinforced by NFC (NR-NFC).

NR-NFC 1%	NR-NFC 2.5%	NR-NFC 7.5%	NR-NFC 10%	NR-NFC 15%	Assignement
Zone	**1,500–1,200**				
	1,203* (sh)	1,203* (sh)	1,203* (sh)	1,187* (sh)	ν(C-O-C)
1,223 (w)	1,243 (m)	1,241 (m)	1,238 (m)	1,244 (m)	τ(CH$_2$)
1,287 (w)	1,284 (w)	1,280 (w)	1,280 (w)		τ(CH$_2$)
1,313 (w)	1,311 (m)	1,315 (m)	1,315 (m)	1,311 (m)	δ(CH)/ δ(OH)
1,322* (sh)	1,331* (sh)	1,336* (sh)	1,336* (sh)		δ(CH)
1,358 (m)	1,359 (m)	1,360 (m)	1,360 (m)	1,357 (m)	δ(CH$_3$)
1,375 (s)	1,375 (s)	1,375 (s)	1,375 (s)	1,376 (s)	δ(CH$_3$)
1,403* (sh)	1,402* (sh)	1,403* (sh)	1,403* (sh)	1,413* (sh)	δ(CH$_3$) + δ(CH)
1,432* (m)	1,434* (m)	1,434* (m)	1,430* (m)		δ(CH$_2$)
1,451* (s)	1,451* (s)	1,451* (s)	1,451* (m)	1,449* (s)	δ(CH$_2$)
				1,462* (sh)	δ(CH$_2$)
Zone	**1,800–1,500**				
1,513 (w)	1,512 (w)	1,513* (w)	1,513* (sh)	-	δ(0-H)
1,540 (m)	1,530 (m)	1,543 (m)	1,544 (m)	1,539 (m)	δ(0-H)
1,550 (m)	1,550 (m)	-	-	-	δ(0-H)
1,582 (m)	1,590* (sh)	1,590 (m)	1,590 (m)	-	δ(0-H)
1,610* (m)	1,610* (m)	1,615* (m)	1,615* (m)	1,610* (m)	ν(C=C)
1,631 (m)	1,632 (m)	1,632(m)	1,634(m)	1,632 (m)	ν(C=C)
1,648* (sh)	1,650(m)	1,647 (m)	1,647(m)	-	ν(C=C)
1,663 (m)	1,664 (m)	1,664 (m)	1,664 (m)	1,663 (m)	ν(C=C)
				1,710 (s)	ν(C=O)
				1,737 (m)	ν(C=O)
				1,766*(sh)	ν(C=O)
Zone	**4,000–3,000**				
3,034 (m)	3,037 (m)	3,022* (sh)	3,022* (sh)	3,035* (sh)	ν(=C-H)
		3,230* (sh)	3,230* (sh)	3,230* (sh)	ν(O-H)
3,294 (m)	3,290 (m)	3,282 (m)	3,280 (m)	3,282 (m)	ν(O-H)
3,345*(w)	3,350 (m)	3,350 (m)	3,350 (m)	3,350 (m)	ν(O-H)
3,415* (w)	3,405* (w)	3,400 (m)	3,400 (m)	3,411 (m)	ν(O-H)
3,510* (sh)	3,480* (sh)	3,500* (sh)	3,500* (sh)	3,480* (sh)	ν(O-H)

w, weak; m, medium, s, strong; sh, shoulder; ν, Str, stretch; δ, bending deformation; τ, twisting; ρ, rocking; s, symmetric; as, antisymmetric, *, fitted values.

and with the increase of percentage of cellulose to 15% we observe a decrease of intensity ratio from 1.2 to 0.6 marking that we have more hydrogen bonds when adding more of CNW. The situation is different for NR reinforced with NFC. There is a rapid change with two bearings marking the increase of hydrogen bonds with the % of cellulose. Indeed, the smaller the intensity ratio, the greater the contribution of the hydrogen bonds, and henceforth the better adhesion NR/NFC. This result is in very good agreement with the previous characterizations realized to these materials, by means of Scanning Electron Microscopy (SEM), water uptake tests, Dynamic Mechanical Analysis (DMA) [5,15] and by dielectric spectroscopy, in which the authors found that entities (residual lignin and hemicelluloses) surrounding NFC limit water infiltration at filler–matrix interface, increase the tensile modulus, decrease the deformation at break, and increase the storage modulus E'. Moreover, CNWs produce more interfaces with NR, and thus the trapped charges at interface are more important for CNW-based nanocomposites. Therefore, the interfacial polarization appears more intense and in terms of conductivity these entities restrict the interfacial pathway for charge carriers and limit their motion so charge carriers movements could be easier at the NR-CNW interfaces [6,14,30,31]. All these characterizations confirmed the conclusion that the interfacial adhesion in the case of NFC/NR nanocomposite is higher than that of NR/CNW one. Figure 4 is a schematic illustration of both the NR-NFC and NR-CNW interfaces. It is well known that CNWs and NFCs

TABLE 4. Summary of changes in functional group band intensity for NR-CNW and NR-NFC.

Group	Location (cm^{-1})	NR-CNW		NR-NFC		
		1→5%	5→15%	1→2.5%	2.5→7.5%	7.5→15%
ν(=C-H)	3,035	–	–	–	–	–
ν(O-H)	3,284	–	↑ ↑ ↑	–	↑ ↑ ↑	↓
ν(O-H)	3,350	–	↑ ↑ ↑	–	↑ ↑ ↑	↓

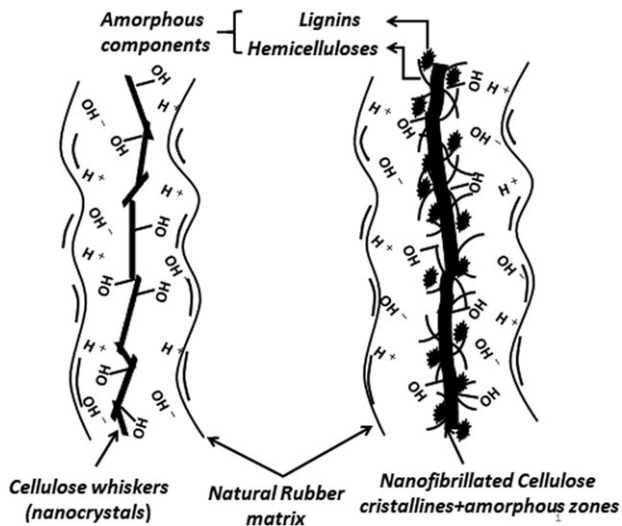↓/↑, weak;↓ ↓ / ↑ ↑, moderate, ↓ ↓ ↓ / ↑ ↑ ↑, strong changes; −, no change (stable).

FIG. 4. Schematic illustration of the NR-CNW (a) and NR-NFC (b) interfaces

show substantially different shapes, composition and sizes. As observed, NFC surface is covered by residual lignin and hemicelluloses while CNW surface is free from these entities and contains only cellulose chains. The reasons for the changed interfacial adhesion cannot be dissociated from the nature of the surfaces involved. Thus, the surface strongly conditions the possibilities of chemical or physical bonds representing adhesion to the interface between two materials. In fact, lignin present in the NFC surface contains [32] polar (hydroxyl) groups and nonpolar hydrocarbon and benzene rings, it is expected to be able to improve the adhesion between the two components of the composite, acting as a compatibilizer between hydrophilic natural fiber reinforcement and hydrophobic matrix polymer [33]. Some attempts to utilize lignin as a compatibilizer in various polymeric systems have been documented in different works [34–36].

In addition, the area within the peak is a very important parameter to be considered in this context. Figure 5a and b shows the area within the peaks at 3,035, 3,284, and 3,350 cm^{-1} as a function of % of CNW and % of NFC, respectively. For NR-CNW, between 1 and 7.5%, the area

remains practically stable for all peaks. Then, after 7.5% of CNW, we observe a fast rise of these areas for both peaks located at 3,284 and 3,350 cm^{-1} corresponding to ν(O-H) stretching modes. The evolution of this Area is agreed with the previous observation made within intensity ratio variation in the case of NR-CNW. This result confirms again that we have more hydrogen bonds when adding more of CNWs. For NR-NFC, we have also a fast rise of area for the same peaks but from 2.5% of NFC. This rise indicates the significant interactions between the matrix NR and NFC from a low rate of reinforcement compared with NR–CNW and therefore the better adhesion NR/NFC.

In the Spectral Region 1,800–1,500 cm^{-1}. Figure 6a and b, where both spectra were normalized on the mode at 1,664 cm^{-1}, show respectively the FTIR spectra of the composites NR–CNW and NR–NFC. For NR–CNW samples, the IR spectra in this spectral region can be separated in two parts: between 1,800 and 1,610 cm^{-1} and between 1,610–1,500 cm^{-1}. The first part corresponds to two vibrational modes at 1,650 and 1,664 cm^{-1} associated only to C=C stretching vibration of NR matrix whereas the second part reveals the δ(O-H) bending modes due to the cellulose. For NR-CNW 1%, NR-CNW 2.5%, and NR-CNW 15%, these two parts have similar intensities whereas for NR-CNW 5% and NR-CNW 7.5%, the ν(C=C) stretching modes are more intense than the δ(O-H) bending modes.

For the NR-NFC samples, the changes are more spectacular. Until NR-NFC 10%, we remark the same distribution of IR spectra in this spectral region in two parts between 1,800 and 1,610 cm^{-1} and between 1,610 and 1,500 cm^{-1}. The first part corresponds to four vibrational modes at 1,610, 1,631, 1,650, and at 1,664 cm^{-1}, the first two peaks are associated only to C=C stretching vibration of lignin [37] whereas the last two peaks are assigned to C=C stretching vibration of NR matrix. Moreover, for NR-NFC 15% (see Fig. 6b), we can distinguish three vibrational parts: a new part between 1,800 and 1,700 cm^{-1} assigned to the carbonyl stretching mode ν(C=O). From Table 3, we can note three additional modes at 1,765, 1,737, and
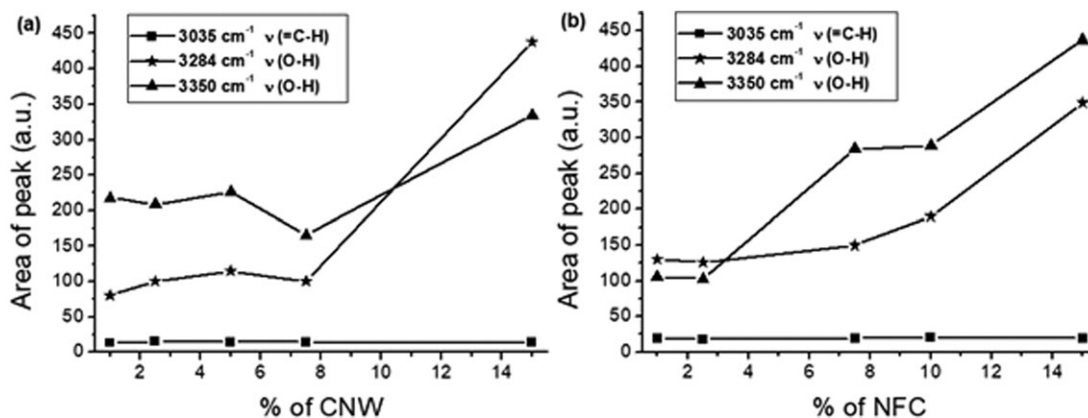

FIG. 5. Variation of Area under the peaks located at 3,035, 3,284, and 3,350 cm^{-1} as a function of reinforcement rate for (a) NR-CNW and (b) NR-NFC nanocomposites.
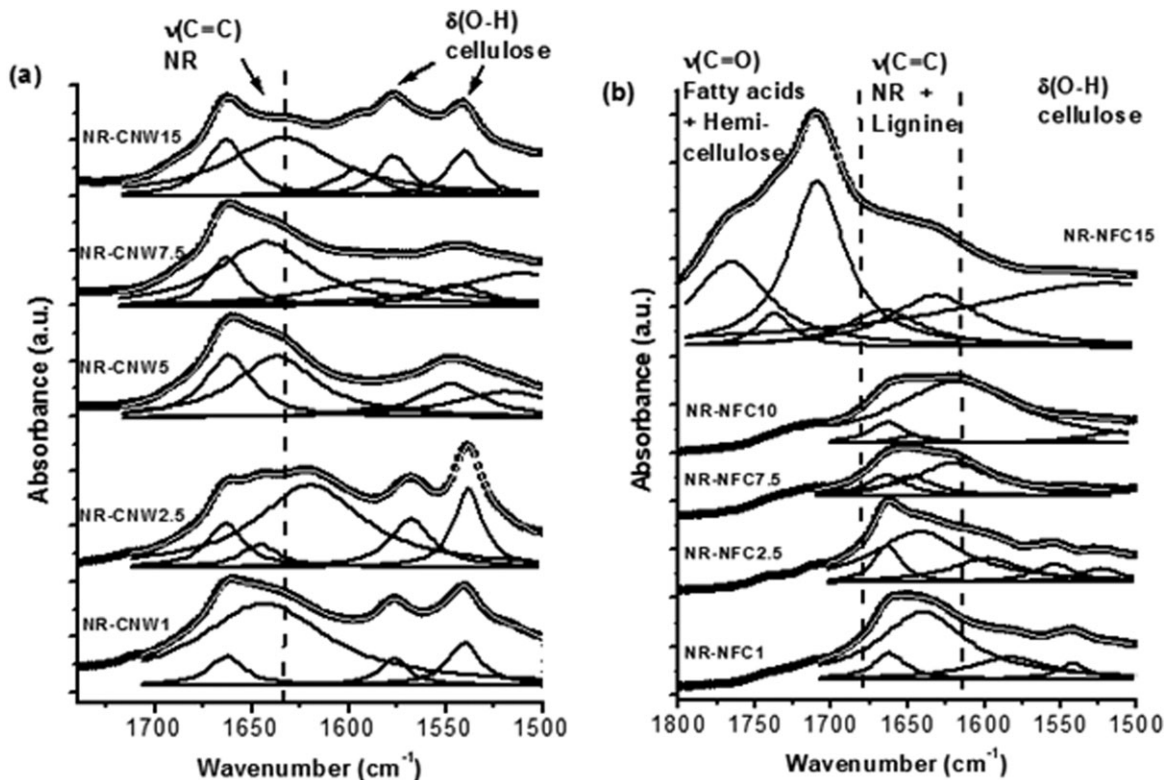
FIG. 6.   IR spectra of (a) NR-CNW and (b) NR-NFC nanocomposites in the spectral region from 1,500 to 1,800 cm^{-1}, fitted by Lorentzian curves as a function of reinforcement rate.

1,710 cm^{-1}, with very important intensities. Nevertheless, the NR and the cellulose do not possess C=O carbonyl group in their structures. These C=O stretching modes in the NR-NFC 15% IR spectrum can be explained by the presence of both hemicelluloses and fatty acids at the surface of NFC lignin [37]. The residual lignin, hemicelluloses, and fatty acids give the hydrophobic character to the NR-NFC contrary to the NR-CNW which has an hydrophilic character as we said previously, the CNW surface is free from these entities and contains only cellulose chains. This result is correlated with the dielectric one in which the authors found that water relaxation of NR-CNW nanocomposites seems more intense compared to NR-NFC nanocomposites and it was explained also by the difference in the structure and composition of both nanoparticles and in particular by the presence of residual lignin, hemicelluloses, extractive substances and fatty acids at the surface of NFC that limits, comparatively, the hydrophilic character of the nanofiller [14,24,38].

In order to show the impact of lignin and to evaluate the intensity contribution of the cellulose into NR –matrix we present in Fig. 7 the intensity ratio $I_{1,630}/I_{1,650} = I(\nu_{(C=C)}/I(\nu_{(C=C)})$ as the mode at 1,630 cm^{-1} is related only to the lignin present at the NFC surface and in opposite the mode at 1,650 cm^{-1} is related only to the NR matrix. From Fig. 7, we observe that intensity ration quickly rise between 2.5 and 10% of NR-NFC and for NR-NFC15%, we note an important decrease of this intensity ratio. This result confirms that lignin plays an important role in the NR-NFC adhesion mechanism.

In the Spectral Region 1,500–1,200 cm^{-1}.   In this spectral region, we observe several wide peaks assigned to $\delta(CH)$, $\delta(CH_2)$, $\delta(CH_3)$, and $\delta(O-H)$ deformation modes (see Fig. 8a and b, where both spectra were normalized on the mode at 1,310 cm^{-1}).

From Tables 2 and 3, we can distinguish four particular modes at 1,450, 1,375, 1,310, and 1,203 cm^{-1} corresponding respectively to $\delta(CH_2)$, $\delta(CH_3)$, $(\delta(CH)+\delta(O-H))$ deformation modes and $\nu(C-O-C)$ stretching mode. Concerning the intensity of these modes, as observed in Table 5 we remark that their intensities seem to be constant more or less as function of reinforcement rate in the case of NR-
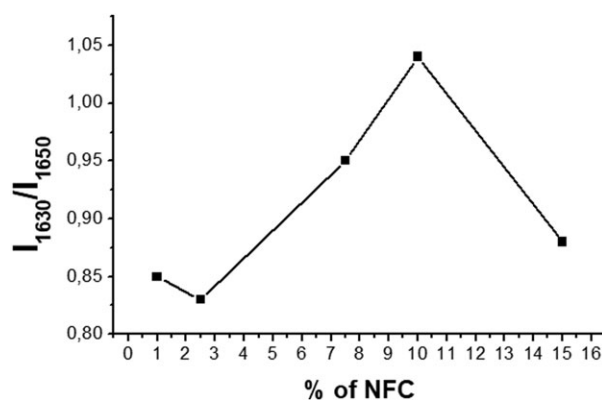

FIG. 7.   Intensity ratios $I_{1,630}/I_{1,650}$ as a function of reinforcement rate for NR-NFC nanocomposites.
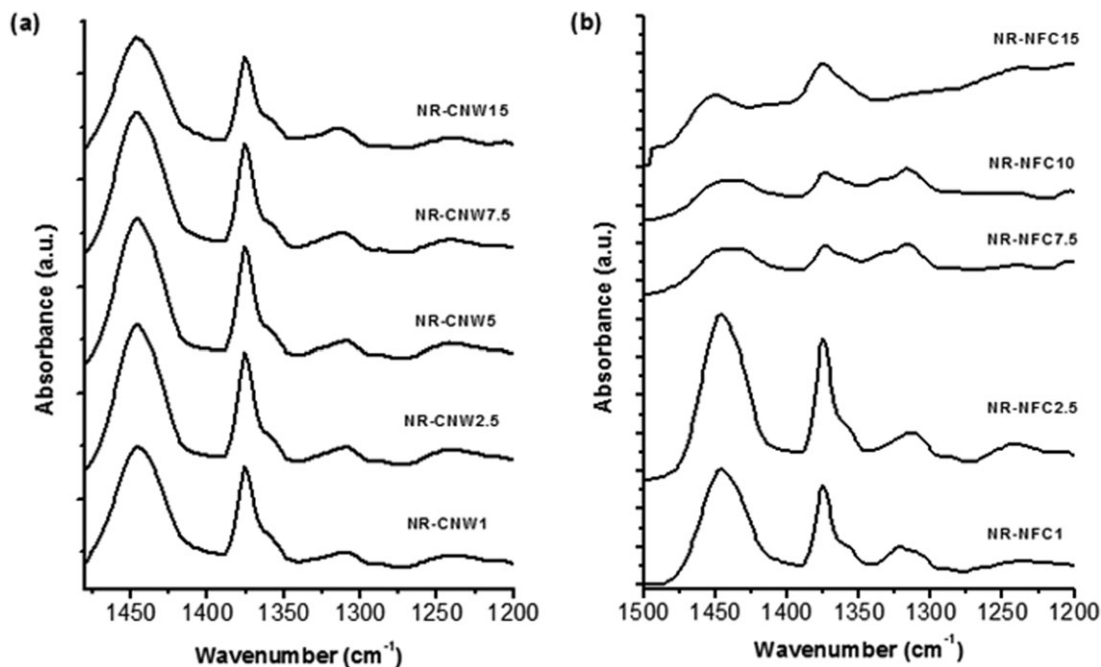
FIG. 8. IR spectra of (a) NR-CNW and (b) NR-NFC nanocomposites in the spectral region from 1,200 to 1,500 cm^{-1}.

CNW whereas for NR-NFC, a significant variation of intensity is observed .

In order to evaluate these changes, the intensity ratios $I_{1,310}/I_{1,375} = I_{(\delta_{(CH)} + \delta_{(O-H)})} / I_{(\delta_{(CH3)})}$ and $I_{1,203}/I_{1,375} = I_{(\nu_{(C-O-C)})} / I_{(\delta_{(CH3)})}$ as a function of reinforcement rate were described in Fig. 9a and b for NR-NFC. These intensity ratios can be served to evaluate the intensity contribution of the cellulose into the NR-CNW and NR-NFC matrix because the modes at 1,310 and 1,203 cm^{-1} are assigned to δ(O-H) deformations existing only for the cellulose and in opposite of the mode at 1,375 cm^{-1} corresponding to the δ(CH3) bending mode existing only for NR–matrix. All the intensity ratios quickly rise between 2.5 and 10% of NR-NFC. For $I_{1,310}/I_{1,375}$, the intensity ratio passes from 0.45 to 1.05 for NR-NFC, from 0.10 to 1.40 for $I_{1,203}/I_{1,375}$ whereas for NR-CNW these two intensity ratios do not practically vary. For NR-NFC 15%, we note an important decrease of these two intensity ratios. This result indicates the contribution of the C-O stretching of the aryl group in lignin [39] and the absence of this contribution for NR-CNW is due to the acid hydrolysis treatment which removes the amorphous regions (hemicellulose and lignin) of the fiber leaving intact the crystalline fraction [30,39,40].

In the Spectral Region 1,200–600 cm^{-1}. In this spectral zone, we note in the Fig. 10a three particular modes: two vibrational modes characterized the cellulose at 1,058 and 1,030 cm^{-1} assigned to ν(C-OH) stretching mode and one mode at 841 cm^{-1} corresponded to ρ(CH3) rocking mode existing only for NR–matrix. Figure 10b and c, where both spectra were normalized on the mode at 841 cm^{-1}, show respectively the FTIR spectra of the composites NR-CNW and NR-NFC. From these figures, we can distinguish two vibrational parts: between 1,200 and 900 cm^{-1} dominated by the cellulose vibrational modes and between 900 and 800 cm^{-1} dominated by the NR ρ(CH3) rocking mode at

TABLE 5. Summary of changes in functional group band intensity for NR-CNW and NR-NFC.

Group	Location (cm^{-1})	NR-CNW				NR-NFC			
		1→2.5%	2.5→5%	5→7.5%	7.5→15%	1→2.5%	2.5→7.5%	7.5→10%	10→15%
ρ(CH$_3$)	841	–	–	–	–	–	–	↓	–
ν(C-O)	1,058	↑	↓	↑	↑↑	↓	↑↑↑	↑	↓↓
ν(C-O)	1,030	↑	↓	↑	↑↑	↓	↑↑↑	↑	↓↓
δ(CH$_3$)	1,375	–	–	–	–	–	–	–	–
δ(0-H)	1,310	↑↑	↓↓	↑	↑↑	↓	↑↑↑	↑	↓↓
δ(0-H)	1,203	↓	↓	↑	↑↑	↓↓	↑↑↑	↑↑	↓↓
ν(C=O)	1,710	∅	∅	∅	∅	∅	∅	∅	↑↑↑
ν(C=O)	1,737	∅	∅	∅	∅	∅	∅	∅	↑↑
ν(C=O)	1,765	∅	∅	∅	∅	∅	∅	∅	↑

↓/↑, weak;↓ ↓ / ↑ ↑, moderate, ↓ ↓ ↓/↑ ↑ ↑, strong changes; −, no change (stable).
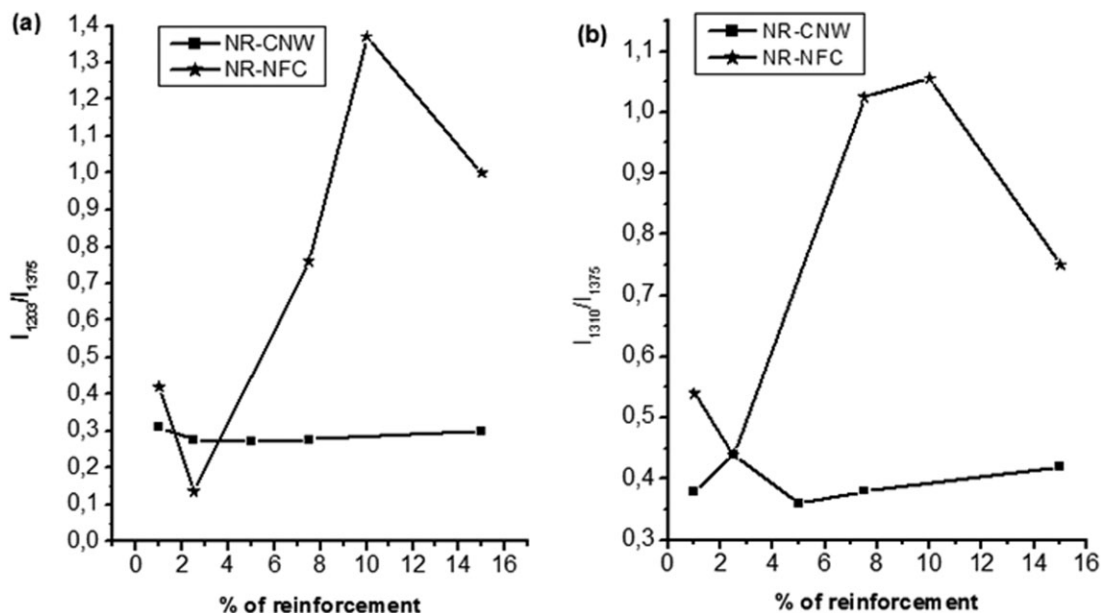
FIG. 9. Intensity ratios (a) $I_{1,203}/I_{1,375}$ and (b) $I_{1,310}/I_{1,375}$ as a function of reinforcement rate for NR-CNW and NR-NFC nanocomposites.

841 cm^{-1}. For NR-CNW, we observe a change for the first part only for NR-CNW 15% with the appearance of two resolved peaks assigned to ν(C-OH) stretching mode at 1,058 and 1,030 cm^{-1}. According to the percentage of reinforcement, these two parts have similar intensities. In opposite, for NR-NFC nanocomposites, from 7.5% of cellulose, we observe an inversion of intensity between both parts: the first part increases significantly in intensity. A summary of changes in the intensity of these functional group band is presented in table 5 for NR-CNW and NR-NFC.

In order to evaluate these intensities, we introduce in Fig. 11a–c three intensity rations: $I_{1,058}/I_{841} = I_{(\nu(C-O))} / I_{(\rho(CH3))}$, $I_{1,030}/I_{841} = I_{(\nu(C-O))} / I_{(\rho(CH3))}$ and $I_{1,030}/I_{1,058} = I_{(\nu(C-O))} / I_{(\nu(C-O))}$. For NR-CNW, these three intensity ratios

do not seem to change whereas for NR-NFC we observe a very strong increase for the two ratios $I_{1,058}/I_{841}$ and $I_{1,030}/I_{841}$ until 10% of reinforcement (from 1.0 to 4.0) then a decrease of these ratios for NR-NFC 15% (from 4.0 to 2.0).

Similar behavior was observed using dielectric analysis; [6] the interfacial polarization strength increases with filling, the number of free charges trapped at the interface increases with the filler content. From a critical NFC rate (between 2.5 and 7.5 wt%), the interface become sufficiently charged, and the interactions between the dipoles become more important and then this is reflected by a decrease in the polarization intensity indicating a rigid interface. We observe the same phenomenon from the study of the intensity ratios $I_{1,058}/I_{841}$ and $I_{1,030}/I_{841}$ as a
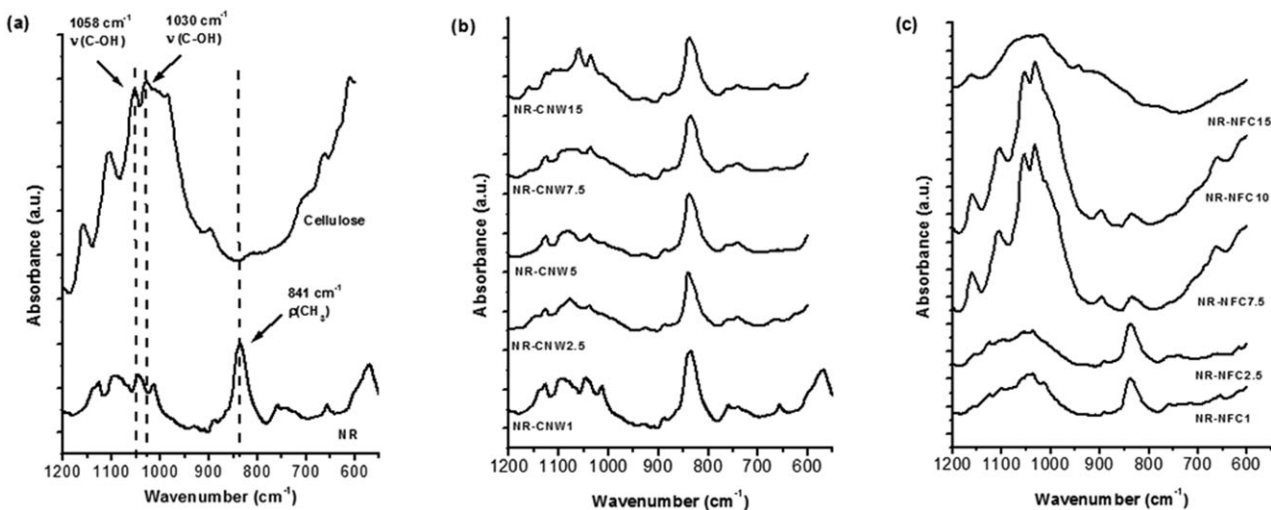

FIG. 10. IR spectra of (a) NR matrix and Cellulose and (b) NR-CNW and (c) NR-NFC nanocomposites in the spectral region from 600 to 1,200 cm^{-1}
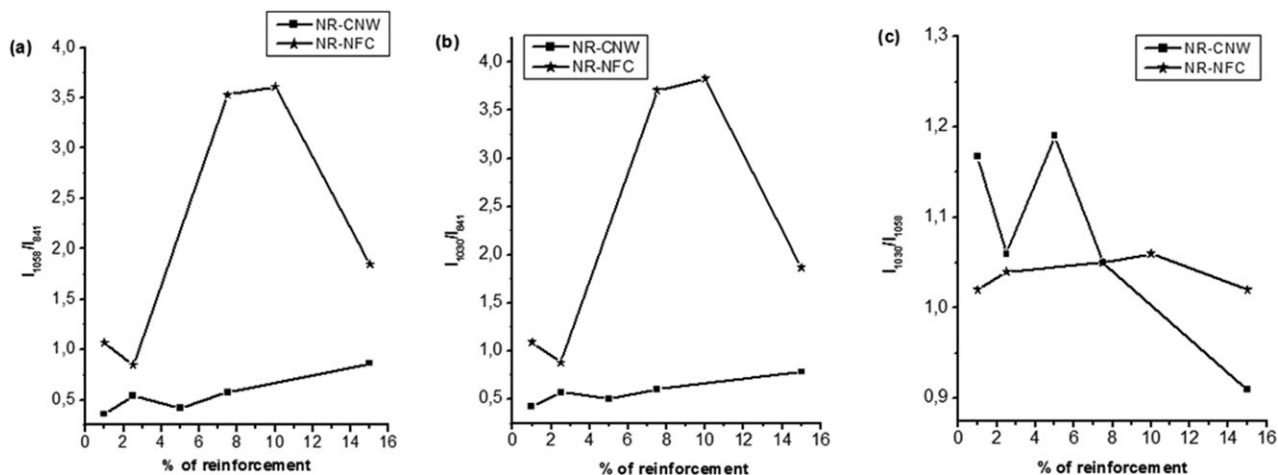
FIG. 11. Intensity ratios (a) $I_{1,058}/I_{841}$, (b) $I_{1,030}/I_{841}$, and (c) $I_{1,030}/I_{1,058}$ as a function of reinforcement rate for NR-CNW and NR-NFC nanocomposites.

function of NFC rate, but we observe a threshold value at 10% of NFC. For NR-NFC, the intensity ratio $I_{1,030}/I_{1,058}$ does not seem to change, so these two peaks evolve in intensity in the same way according to the percentage of cellulose. Thus, these two peaks are assigned to the vibrational behavior of the cellulose. Other studies on NR-CNW appear important [41–44].

SUMMARY AND CONCLUSION

In this work, we have investigated infrared spectra performed on NR isolated from Hevea Brasiliens and its composites using CNWs and NFC extracted from the rachis of date palm tree, by means infrared spectroscopy at room temperature and in the spectral range 4,000–600 cm^{-1}. In the spectral regions 3,500–2,600, 1,800–1,500, 1,500–1,200, and 1,200–600 cm^{-1}, many vibrational modes were found to be important witnesses of structural changes when adding cellulose nanoparticles into NR matrix. These vibrational changes are manifested by shifts in frequency, significant variations in the intensity and the appearance or disappearance of vibrational modes from a precise value of reinforcement rate. In a general way, the NR-NFC is much more sensitive to the vibrational changes according to the percentage of cellulose into the NR–matrix than the NR-CNW samples. In the spectral range 3,500–2,600 cm^{-1}, the study of the intensity ratio $I_{3,035}/I_{3,350} = I_{\nu(=C-H)}/I_{\nu(C-OH)}$ according to the percentage of cellulose for NR-CNW and NR-NFC shows a reduction of this ratio from 7.5% of cellulose for NR-CNW whereas for NR-NFC this decrease begins with a lower percentage of cellulose. This phenomenon is explained by the difference in the structure of both nanoparticles and in particular by the presence of residual lignin and hemicelluloses at the surface of NFC that limits, comparatively, the hydrophilic character of the nanofiller. In the spectral range 1,800–1,500 cm^{-1}, this presence of lignin is confirmed by the appearance of the C=O stretching mode for the NR-NFC 15% IR spectrum. In the spectral range 1,500–600 cm^{-1}, the studies of four intensity ratios ($I_{1,310}/I_{1,375}$, $I_{1,203}/I_{1,375}$, $I_{1,058}/I_{841}$, and $I_{1,030}/I_{841}$) have permitted us to show an important impact on the vibrational behavior according to the percentage of cellulose for NR-NFC samples: we observe a strong increase from 1 to 10% of reinforcement then a decrease for 15%. All these results confirm our dielectric analysis on the same samples for which it had been established that the lignins play the role of "compatibilizing" agent that enhance the adhesion between NR matrix and the NFC. Overall, the objectives of this work were focused on the understanding of the incorporation effect of cellulosic nanoparticles with different forms and mass fractions on the vibrational properties of the nanocomposite materials.

REFERENCES

1. M. Grunert, W.T. Winter, and J. Polym, *Environ.*, **10**, 27 (2002).

2. K. Oksman, A.P. Mathew, D. Bondeson, and I. Kvien, *Compos Sci Technol*, **66**, 2776 (2006).

3. Fernanda Abbate dos Santos, C. V. Gisele Iulianelli, and Maria Inês Bruno Tavares, *Mater Sci Appl* **7**, 257–294 (2016).

4. A. Bendahou "Nouveaux Matériaux Nanocomposites à Base de Monocristaux de Cellulose et de Polymère : Relation Structure – Propriétés" Thesis in Chemistry, Université Cadi ayyad (2009).

5. A. Bendahou, H. Kaddami, and A. Dufresne, *Eur. Polym. J.*, **46**, 609 (2010).

6. A. Ladhar, M. Arous, H. Kaddami, M. Raihane, A. Kallel, M.P.F. Graça, and L.C. Costa, *J. Mol. Liq.*, **196**, 187 (2014).

7. F. Agrebi, N. Ghorbel, A. Ladhar, S. Bresson, and A. Kallel, *Materials Chemistry and Physics*, **200**, 155 (2017).

8. Y.R. Hu, J.K. Liang, A.S. Myerson, and L.S. Taylor, *Ind. Eng. Chem. Res.*, **44**, 1233 (2005).

9. G. Schoukens and K. De Clerck, *Polymer*, **46**, 845 (2005).

10. S. Bresson, M. El Marssi, and B. Khelifa, *Vib. Spec.*, **40**, 263 (2006).

11. M. EL Hadri, A. Achahbar, J. El Khamkhami, B. Khelifa, V. Faivre, C. Tran Le Tuyet, O. Abbas, M. El Marssi, F. Bougrioua, and S. Bresson, *Journal of Molecular Structure*, **1083**, 441 (2015).

12. S. Bresson, D. Rousseau, S. Ghosh, M. E. Marssi, and V. Faivre, *Eur. J. Lipid Sci. Technol*, **113**, 992 (2011).

13. W. Gindl-Altmutter, M. Obersriebnig, S. Veigel, and F. Liebner, *ChemSusChem* **8**, 87–91 (2015).

14. A. Ladhar, M. Arous, H. Kaddami, M. Raihane, A. Kallel, M.P.F. Graça, and L.C. Costa, *J. Mol. Liq.*, **211**, 792 (2015).

15. A. Bendahou, Y. Habibi, H. Kaddami, A. Dufresne, and J. Biobased Mater, *Bioenergy*, **3**, 81 (2009).

16. S. Bresson, M. El Marssi, and B. Khelifa, *Chem Phys Lipids.*, **134**, 119 (2005).

17. M. Adam Healy, J. Patrick Hendra, and D. Yvonne West, *Polymer*, **37**, 4009 (1996).

18. D.P. Li-Ling Cho and B.S. Kai-Bin Huang, *Forensic Science Journal*, **11**, 33 (2012).

19. E. Abraham, B. Deepa, L. A. Pothan, Maya John, S. S. Narine, S., Thomas, and R. Anand jwala, *Cellulose*, **20**, 417–427 (2013).

20. G. Socrates. Infrared and Raman Characteristic Group Frequencies: Tables and Charts. John Wiley & Sons, The University of West London, UK 347 (2004).

21. Y. Maréchal and H. Chanzy, *J. Mol. J. Struct*, **523**, 183 (2000).

22. M. Sain, and S. Panthapulakkal, *Indust Crops and Products*, **2**, 1–8 (2006).

23. C.Y. Liang and R.H. Marchessault, *Journal of Polymer Science*, **37**, 385 (1959).

24. A. Bendahou, H. Kaddami, M. Raihan, A. Dufresne, and Y. Habibi, *Revue Roumaine de Chimie*, **54**, 571 (2009).

25. X. Colom, F. Carrasco, P. Pagès, and J. Canavate, *Compos. Sci.Technol.*, **63**, 161 (2003).

26. A. Alemdar and M. Sain, *Bioresource Technology*, **99**, 1664 (2008).

27. X. Xu, F. Liu, L. Jiang, J.Y. Zhu, D. Haagenson, and P. Dennis Wiesenborn, *ACS Appl. Mater. Interface*, **5**, 2999 (2013).

28. J.F. Kadla and S. Kubo, *Macromolecules*, **36**, 7803 (2003).

29. T. Kondo, C. Sawatari, and D.G. Gray, *Macromolecules*, **27**, 210 (1994).

30. A. Ladhar, M. Arous, H. Kaddami, M. Raihane, M. Lahcini, A. Kallel, M.P.F. Graça, and L.C. Costa, *J. Non-Cryst. Sol.*, **378**, 39 (2013).

31. A. Ladhar, A. Bendahou, M. Arous, A. Dufresne, and H. Kaddami, "Dielectric Spectroscopy: An Efficient Tool to Study the Interfacial Adhesion and Properties of Natural Rubber/Nanocellulose-Based Green Nanocomposites", in Handbook of Nanocellulose and Cellulose Nanocomposites, Wiley-VCH Verlag GmbH & CO, KGaA, Weinheim, Germany 627–648 (2017).

32. D. Feldman, D. Banu, J. Campanelli, and H.J. Zhu, *Appl Polym Sci.*, **81**, 861 (2001).

33. W. Thielemans and R.P. Wool, *Compos A*, **35**, 327 (2004).

34. H.D. Rozman, K.W. Tan, R.N. Kumar, A. Abubakar, Z. A. Mohd Ishak, and H. Ismail, *Eur Polym J*, **36**, 1483 (2000).

35. H.D. Rozman, K.W. Tan, R.N. Kumar, and A. Abubakar, *J Appl Polym Sci*, **81**, 1333 (2001).

36. C. Pouteau, P. Dole, B. Cathala, L. Averous, and N. Boquillon, *Polym Degrad Stab*, **81**, 9 (2003).

37. H. Yang, R. Yan, H. Chen, D. Ho Lee, and C. Zheng, *Fuel*, **86**, 1781 (2007).

38. A. Dufresne, J.Y. Cavaillé, and M.R. Vignon, *J. Appl. Polym. Sci.*, **64**, 1185 (1997).

39. K. Benhamoua, H. Kaddami, A. Magnind, A. Dufresne, and A. Ahmade, *Carbohydr Polym*, **122**, 202 (2015).

40. C.D. Edgar and D.G. Gray, *Cellulose*, **10**, 299 (2003).

41. X. Wu, C. Lu, H. Xu, X. Zhang, and Z. Zhou, *ACS Appl. Mater. Interfaces*, **23**, 21078 (2014).

42. X. Liu, G. Su, Q. Guo, C. Lu, T. Zhou, C. Zhou, and X. Zhang, *Adv. Funct. Mater.*, **28**, 1706658 (2018).

43. J. Cao, C. Lu, J. Zhuang, M. Liu, X. Zhang, Y. Yu, and Q. Tao, *Angew .Chem. Int.Ed.*, **56**, 8795 (2017).

44. X. Wu, C. Lu, X. Zhang and Z. Zhou , *J. Mater. Chem. A.* **3**, 13317–13323 (2015).